Luminescent Er 3+ based single molecule magnets with fluorinated alkoxide or aryloxide ligands

Alexander Selikhov, Gautier Félix, Dmitry Lyubov, Yulia Nelyubina, Anton Cherkasov, Saad Sene, Ilya Taydakov, Mikhail Metlin, Andrey Tyutyunov, Yannick Guari, et al.

Luminescent Er^{3+} Based Single Molecule Magnets with Fluorinated Alkoxide or Aryloxide Ligands

Alexander A. Selikhov,[a,b] Gautier Félix,[c] Dmitry M. Lyubov,[a,b] Yulia V. Nelyubina,[a] Anton V. Cherkasov,[b] Saad Sene,[c] Ilya V. Taydakov,[d,e] Mikhail T. Metlin,[d] Andrey A. Tyutyunov,[a] Yannick Guari,[c] Joulia Larionova*[c] and Alexander A. Trifonov*[a,b]

a. A. N. Nesmeyanov Institute of Organoelement Compounds of Russian Academy of Sciences, 28 Vavilova str., 119334, Moscow, Russia.

b. Institute of Organometallic Chemistry of Russian Academy of Sciences, 49 Tropinina str., GSP-445, 630950, Nizhny Novgorod, Russia.

c. ICGM, Univ. Montpellier, CNRS, ENSCM, Montpellier, France.

d. P. N. Lebedev Physical Institute of the Russian Academy of Sciences, Leninskiy Prospect 53, 119991, Moscow, Russia

e. N. D. Zelinsky Institute of Organic Chemistry Russian Academy of Sciences, Leninsky Prospect, 47, 119991, Moscow, Russia

We report the synthesis, structures, magnetic and luminescent properties of a series of new mono- and dinuclear Er^{3+} complexes derived from sterically demanding aryloxide and fluorinated alkoxide ligands: [4-*t*Bu-2,6-$(Ph_2CH)_2C_6H_2O]_3Er(THF)$ (**1**), $[(C_6F_5)_3CO]_3Er(Me_3SiOH)$ (**2**), $[(C_6F_5)_3CO]_3Er[(Me_3Si)_2NH]$ (**3**), $[(C_6F_5)_3CO]_3Er(C_6H_5CH_3)$ (**4**), $[(C_6F_5)_3CO]_3Er(o\text{-}Me_2NC_6H_4CH_3)$ (**5**) and $\{[Ph(CF_3)_2CO]_2Er(\mu^2\text{-}OC(CF_3)_2Ph]\}_2$ (**6**). In compounds **1**, **2**, and **4**, Er^{3+} ion is four-coordinated and adopts a distorted trigonal pyramidal geometry, while in **3**, **5**, and **6**, the coordination geometry of Er^{3+} is impacted by the presence of several relatively short Er…F distances making them rather 6-coordinated. All compounds behave as field-induced Single Molecule Magnets (SMMs) and exhibit an Er^{3+} characteristic near infrared (NIR) emission associated with $^4I_{13/2}\rightarrow{}^4I_{15/2}$ transition with a remarkable long lifetime going up to 73 µs, which makes them multifunctional luminescent SMMs. The deconvolution of the NIR emission spectra allowed to provide a direct probe of the crystal field splitting in these compounds, which was correlated to magnetic data.

Introduction

Lanthanide ions-based coordination compounds have undergone significant development thanks to the relatively recent discovery of mononuclear dysprosium metallocenes family presenting a Single Molecule Magnetic (SMM) behavior occurring at temperatures near the boiling point of liquid nitrogen.[1–4] It has unveiled new interesting possibilities for employing SMMs in different applications aiming to achieve miniaturization, such as spintronic devices, quantum computing, and data storage.[5–7] The observation of this phenomenon is attributed to the presence of high magnetic anisotropy and large magnetic moments of lanthanide ions in the appropriate coordination environments, permitting them to exhibit slow magnetic relaxation and a molecular-level magnetic hysteresis effect. This discovery has spurred significant progress in designing numerous mono- and polynuclear lanthanide-based complexes, primarily centered around the Dy^{3+} ion, and the rational optimization of their magnetic properties.[8–13] Indeed, Dy^{3+} emerges as the prime candidate for developing high-performance SMMs. Its Kramers nature, doubly degenerate ground state, and oblate shape contribute to a robust magnetic ground spin state, ensuring a well-separated ground and first excited state critical for strong magnetic anisotropy. This distinctive combination has encouraged extensive research on Dy^{3+}-based SMMs, resulting in the development of highly efficient magnets with large energy barriers and elevated blocking temperatures exceeding, in some cases, the freezing point of liquid nitrogen. Comparatively, and within the spectrum of different lanthanide ions, SMMs built with Er^{3+} ion are notably scarcer. Nevertheless, the persistent growth in literature dedicated to this topic underscores a purposeful and strategic approach. With a m_J value of ± 15/2 derived from $^6H_{15/2}$ multiplets, the Er^{3+} ion exhibits a pronounced electronic distribution according to the so-called "oblate-prolate" model. This latter posits a prolate configuration, attainable through the coordination of ligands in the equatorial plane. Two different strategies have been used to enhance uniaxial anisotropy and mitigate Quantum Tunneling of Magnetization (QTM) in design of Er^{3+} SMM. The first one consists in the synthesis of organometallic sandwich complexes, specifically those incorporating rich-π cyclooctatriene (COT^{2-}) or 1,4-bis(trimethylsilyl) cyclooctatetraenyl (COT''^{2-}) dianions, which house the most efficient mononuclear Er^{3+} based SMMs.[14–21] They create a predominantly equatorial crystal field through the influence of two aromatic ligands, resulting in a slow relaxation of the magnetization with the highest reported energy barriers for mononuclear Er^{3+} SMMs. For example, the compound (Dsp)Er(COT) (where $[Dsp]^-$ = 3,4-dimethyl-2,5-bis(trimethylsilyl)phospholyl)) has been reported to exhibit an energy barrier of 358 K and a blocking temperature of 9 K.[21] The second strategy entails making mononuclear Er^{3+} coordination compounds with deliberately low coordination number, directing the crystal field exclusively in the equatorial plane of the Er^{3+} ion. Notably, the $Er[N(SiMe_3)_2]_3$ compound is the first member of this family. Within this compound, the Er^{3+} ion assumes a triangular coordination geometry, showcasing an energy barrier of 122 K and a blocking temperature of 13 K.[22] Distinguished by their tri-coordinated coordination environment of Er^{3+}, other genuine SMMs based on different sterically encumbering ligands, such as bis(trimethylsilyl)amide,[22,23] cresolate,[24] silyl-based,[24] phenolate[25] or nitrogen carbazolyl[26] have been reported. These SMMs, in contrast to the previously mentioned sandwich compounds, exhibit lower effective energy barriers, while comparable blocking temperatures. This “three-coordination environment strategy” in design of Er^{3+} SMMs has been challenged in light of the magnetic performance exhibited by the first tetra-coordinated Er^{3+} ion in $[Li(THF)_4][Er\{N(SiMe_3)_2\}_3Cl]\cdot 2THF$ presenting a genuine SMM behavior with an

unexpectedly high effective energy barrier of 63.3 K and an hysteresis loop up to 3 K.[27] Indeed, within this compound, the Er^{3+} center assumes a trigonal pyramidal geometry. It is coordinated by three $N(SiMe_3)_2$ moieties, primarily situated in the equatorial plane, and a strictly axial, negatively charged chloride ligand with a notably elongated bond distance. Interestingly, the persistence of a zero-field slow relaxation of the magnetization, despite the presence of the axial chloride, suggests that a strictly prolate f-electron density is not imperative for stabilizing an appropriate crystal field conducive to genuine SMM behavior in Er^{3+}.[23,27] For this reason, other tetra-coordinated SMMs, including $[Er(TTBP)_3(THF)]$ ($TTBP^-$ = 2,4,6-tri-tert-butyl-phenolate), $[Er(BHT)_3(THF)]$ (BHT^- = 2,6-di-tert-butyl-4-methylphenolate) compounds, presenting comparable energy barriers have been reported.[25,28–30] Note also that alternative coordination geometries of Er^{3+} ions with higher coordination numbers (up to 8) have also been reported as SMMs, while the majority of them are field-induced SMMs, involving an application of a static magnetic field to mitigate the QTM process.[27,31–33]

Simultaneously with the optimization of the magnetic performance of lanthanide ions-based SMMs through a deep comprehension of their structure-properties relationship, there has been a growing emphasis on associating SMM behavior with other properties (such as optical, ferroelectric, chirality, and photochromicity etc.) with the goal of creating multifunctional SMMs. Among these, luminescent SMMs have garnered increasing interest not only due to independent observation of both, slow relaxation of magnetization and the characteristic emission of lanthanide ions, but also because the correlation between these functionalities. Indeed, deriving the electronic structures of complexes from their optical properties, such as luminescence, and comparing them with the effective energy barriers identified through dynamic magnetic measurements has, in certain instances, proven crucial for elucidating the mechanisms of magnetic relaxation.[34–37] The literature analysis indicates that the large majority of luminescent SMMs belongs to Dy^{3+}-based and Yb^{3+}-based complexes, trailed at a significant distance, by those involving Tb^{3+} and Er^{3+} ions.[37] The scarcity of luminescent SMMs relying on Er^{3+} can be attributed to the challenges associated with establishing the necessary ligand environment conducive to an effective equatorial crystal field for SMMs and the substantial crystal field splitting involved.[38] The literature indicates that the ligands able to stabilize the equatorial crystal field were inefficient to generate the necessary antenna effect and sensitize Er^{3+} luminescence. In fact, Er^{3+} ion usually presents near infrared (NIR) emission centered at around 1500 nm ($^4I_{13/2} \rightarrow {}^4I_{15/2}$ transition), while its observation is relatively challenging since it can be quenched by different molecular and lattice vibrations.[39] The Er^{3+} ion presents the relatively weak energy gap between the $^4I_{13/2}$ and $^4I_{15/2}$ states of 6000 cm^{-1}, which leads to reduced NIR emission efficiency, caused by the multiphonon quenching effect impacted by several organic fragments occurring in usual antenna ligands (such as O–H, N–H, C–H, C=O, C=N, and C=C bonds).[39] This fact makes difficult to find appropriate ligands to efficiently sensitize this ion and avoid the emission quenching.

The first examples of bifunctional Er^{3+}-based complexes exhibiting both, SMM behavior and efficient luminescence, have been reported in 2014 by using “well known“ β-diketonate antenna ligands.[40,41] The employment of these latter afford designing of 8 or 9-coordinated Er^{3+} complexes with a relatively modest SMM performance: they are field-induced SMMs with the energy barriers of around 20 K. However, β-diketonates efficiently sensitized Er^{3+} ion leading to observance of $^4I_{13/2} \rightarrow {}^4I_{15/2}$ Er^{3+} characteristic emission in the NIR domain. From this date, several other Er^{3+} based luminescent SMMs have also been published, but the examples remain relatively scarce (see Table S1, Electronic Supporting Information (ESI)).[42–51] Upon reviewing the literature, a prevailing trend emerges in the majority of reported cases involving luminescent SMMs based on Er^{3+}. Firstly, in large majority of reported SMMs, Er^{3+} ion typically adopts a conventional eight or nine-coordinated environment. The influence of Er site geometry remains unexplored, with a noticeable absence of strategies focused on designing luminescent SMMs with a low coordination geometry, as it has been done with non-luminescent SMMs. Secondly, the "antenna" ligands utilized face challenges in establishing the necessary equatorial crystal field, as evidenced by frequent occurrence of field-induced luminescent SMMs with effective energy barriers scarcely surpassing ~40 cm^{-1}. Third, only one work reported on the correlation between magnetic relaxation and luminescence for a layered Er^{3+} phosphonate coordination polymer and to the best of our knowledge such correlation has never been reported for mononuclear compounds.[52] In fact, $[Er(notpH_4)(H_2O)]ClO_4{\cdot}3H_2O$ [$notpH_4^{2-}$ = 1,4,7-triazacyclononane-1,4,7-triyl-tris(methylenephosphonate)] compound presented a field induced SMM behavior with the energy barrier of 24.2 cm^{-1} determined by dynamic magnetic measurements under 1000 Oe. The NIR emission was measured at room temperature, and the characteristic $^4I_{13/2} \rightarrow {}^4I_{15/2}$ Er^{3+} transition is observed under the direct Er^{3+} excitation at 1064 nm. The emission spectrum was analyzed using a 10-component multi-Gaussian function, revealing transitions from the Stark splitting of the $^4I_{15/2}$ levels and hot bands. The assignment of these transitions allowed to establish the energy diagram of the Stark sub levels of Er^{3+} and enabled the comparison of the obtained energy gap between the ground and the first excited state of the $^4I_{15/2}$ crystal field splitting of 31.2 cm^{-1} with the effective energy barrier obtained by the dynamic magnetic measurements.[52]

In this article, we report a new series of luminescent Er^{3+}-based SMMs obtained by using bulky phenolate or fluorinated alkoxides combined with complementary ligands in the axial position with the specific goal of achieving a four-coordinated Er^{3+} geometry. Fluorinated ligands proved to be a useful coordination environment allowing designing efficient photo- and electroluminescent materials. Replacement of hydrogens by fluorine atoms improves the luminescence through suppressing the non-radiative deactivation process.[53,54] The pronounced electron withdrawing property of fluorine atoms could also affect the slow relaxation features through alteration of the lanthanide-ligand bonds.[55] Moreover, the presence of fluorine atoms, which are able to form non-covalent interactions (hydrogen bonds, π–π···F interactions, C–F···π interactions, and F···F halogen bonds),[56] might rigidify the molecular structure thus decreasing the Raman relaxation.[57–65] In addition, the presence of non-covalent Er^{3+}···F interactions,

which result in steric and coordination saturation of the metal center, could impede the coordination of other Lewis bases. This hindrance is anticipated to facilitate the stabilization of metal sites with low coordination. By using this strategy, we synthesized three four-coordinate compounds, [4-*t*Bu-2,6-$(Ph_2CH)_2C_6H_2O]_3Er(THF)$ (**1**) and $[(C_6F_5)_3CO]_3Er(Me_3SiOH)$ (**2**), $[(C_6F_5)_3CO]_3Er(C_6H_5CH_3)$ (**4**), wherein the Er^{3+} ion adopts a distorted trigonal pyramidal geometry. In the mononuclear compounds $[(C_6F_5)_3CO]_3Er[(Me_3Si)_2NH]$ (**3**) and $[(C_6F_5)_3CO]_3Er(o\text{-}Me_2NC_6H_4CH_3)$ (**5**), as well as in the di-nuclear complex $\{[Ph(CF_3)_2CO]_2Er(\mu^2\text{-}OC(CF_3)_2Ph]\}_2$ (**6**), the Er^{3+} coordination geometry is impacted by the presence of several relatively short Er···F distances resulting in a trigonal prismatic configuration. All of them behave as field-induced SMMs and exhibit a characteristic Er^{3+} related emission making them luminescent SMMs. The emission spectra of all compounds were exploited to establish the energy diagram of the Stark sublevels and correlate the energy gap between the ground and the first excited states taken from the luminescence with the effective energy barriers obtained from the dynamic magnetic measurements.

Results and discussion

Synthesis and crystal structures

The reaction of $(o\text{-}Me_2NC_6H_4CH_2)_3Er$ with three equivalents of 4-*t*Bu-2,6-$(Ph_2CH)_2C_6H_2OH$ in THF at room temperature (1 h) affords complex [4-*t*Bu-2,6-$(Ph_2CH)_2C_6H_2O]_3Er(THF)$ (1) which was isolated after recrystallization from toluene-hexane mixture in 75% yield (Scheme 1). Complex **1** can be obtained only in the form of a THF adduct, all the attempts to remove the THF molecule by heating in vacuum were unsuccessful. The reaction of $(o\text{-}Me_2NC_6H_4CH_2)_3Er$ with $(C_6F_5)_3COH$ (1:3 molar ratio) in toluene at room temperature allows for the synthesis of complex $[(C_6F_5)_3CO]_3Er(o\text{-}Me_2NC_6H_4CH_3)$ (5) which contains a N-coordinated N,N-dimethyltoluidine molecule released during the reaction. Compound 5 was isolated with 87% yield after recrystallization from toluene-hexane mixture. Both 1 and 5 are absolutely insoluble in aliphatic hydrocarbons, but can be solubilized in more polar solvents, such as toluene or THF.

In this regard, in order to obtain a low-coordinate erbium tris(alkoxide) $[(C_6F_5)_3CO]_3Er$ an amine elimination route consisting in the reaction of a homoleptic tris(amido) precursor $[(Me_3Si)_2N]_3Er$ with $(C_6F_5)_3COH$ was applied (Scheme 2). It was supposed that the formation of $(Me_3Si)_2NH$ featuring rather weak coordination ability due to the shielding of nitrogen pair by bulk TMS-groups and conjugation with a silicon orbital would allow for avoiding coordination with metal center.[66] However, when the reaction was carried out in a non-coordinating solvent heptane ($[(Me_3Si)_2N]_3Er$:$(C_6F_5)_3COH$ molar ratio 1:3), an adduct (**3**) is formed in which the erbium center is coordinated by $(Me_3Si)_2NH$. $(Me_3Si)_2NH$ can be readily replaced by toluene when complex **3** is recrystallized from toluene with 51% yield. If the reaction of $[(Me_3Si)_2N]_3Er$ with $(C_6F_5)_3COH$ was performed in toluene, complex $[(C_6F_5)_3CO]_3Er(C_6H_5CH_3)$ (4) was isolated in 65% yield. The Er^{3+} cation due to the coordination by three electron-withdrawing $(C_6F_5)_3CO$ ligands[67] proved to be highly electrophilic and able to "catch" toluene π-electronic density bonding it in η^6-fashion. The reaction of $[(Me_3Si)_2N]_3Er$ with a five-molar excess of $(C_6F_5)_3COH$ in heptane at 80° C proceeded with hydrolysis of Si-N bonds and afforded a silanol complex $[(C_6F_5)_3CO]_3Er(Me_3SiOH)$ (5). Complexes **2**–**4** are pink crystalline compounds, slightly soluble in aliphatic solvents. Compound **4** loses coordinated toluene upon dissolution in refluxing heptane (according to elemental analysis data), however, all the attempts to obtain crystals suitable for X-ray analysis failed. When less sterically demanding alcohol $Ph(F_3C)_2COH$ was used, the amine elimination reaction with $Er[N(SiMe_3)_2]_3$ (molar ratio 1:3, toluene, r.t.) afforded a dimeric complex $\{[Ph(F_3C)_2CO]_2Er(\mu\text{-}OC(CF_3)_2Ph]\}_2$ (6) (Scheme 2). Most likely, the formation of a dimeric framework due to μ^2-bridging by alkoxide group turned out to be energetically preferable compared to η^6-coordination with toluene.

The single crystal X-ray diffraction study (SC XRD) study revealed that complex **2** crystallizes in the trigonal *R-3* space group, while **1** and **3**–**5** in the triclinic *P-1* space group. (Table S2). The molecular structures of the complexes are shown in Figure 1, while their crystal packings are given in Figures S1 – S6, Electronic Supporting Information (ESI). The coordination environment of the Er^{3+} cation in **1** includes three oxygens from alkoxides and one THF molecule located in the apical position providing distorted trigonal pyramidal geometry (Figure 1a). The $Er\text{–}O_{aryloxide}$ bond lengths are in the narrow interval 2.082(2)–2.094(2) Å, and the $Er\text{–}O_{THF}$ coordination bond is longer and equal to 2.261(2) Å. In **1** a non-valent interaction of one of the phenyl substituents with Er^{3+} is realized, thus resulting in short Er···C distances 2.891(2) and 2.979(2) Å. The erbium cation barely deviates (0.02(2) Å) from the plane defined by three phenoxide oxygen atoms, located equatorially. The $O_{aryloxide}\text{–}Er\text{–}O_{aryloxide}$ angles are in the range 118.01(5)–123.16(5)°, which deviate from the ideal trigonal planar angle of 113.4° for $[Er\{N(SiMe_3\}_3]$. The $O_{THF}\text{–}Er\text{–}O_{aryloxide}$ angles are in the range 86.98(5)–91.71(5)°. The closest intermolecular Er···Er

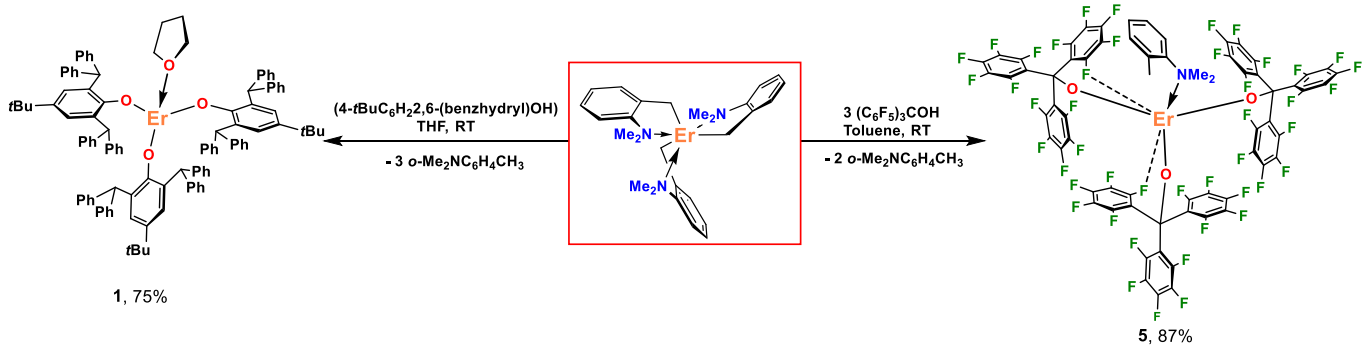

Scheme 1. Synthesis of complexes **1** and **5**.

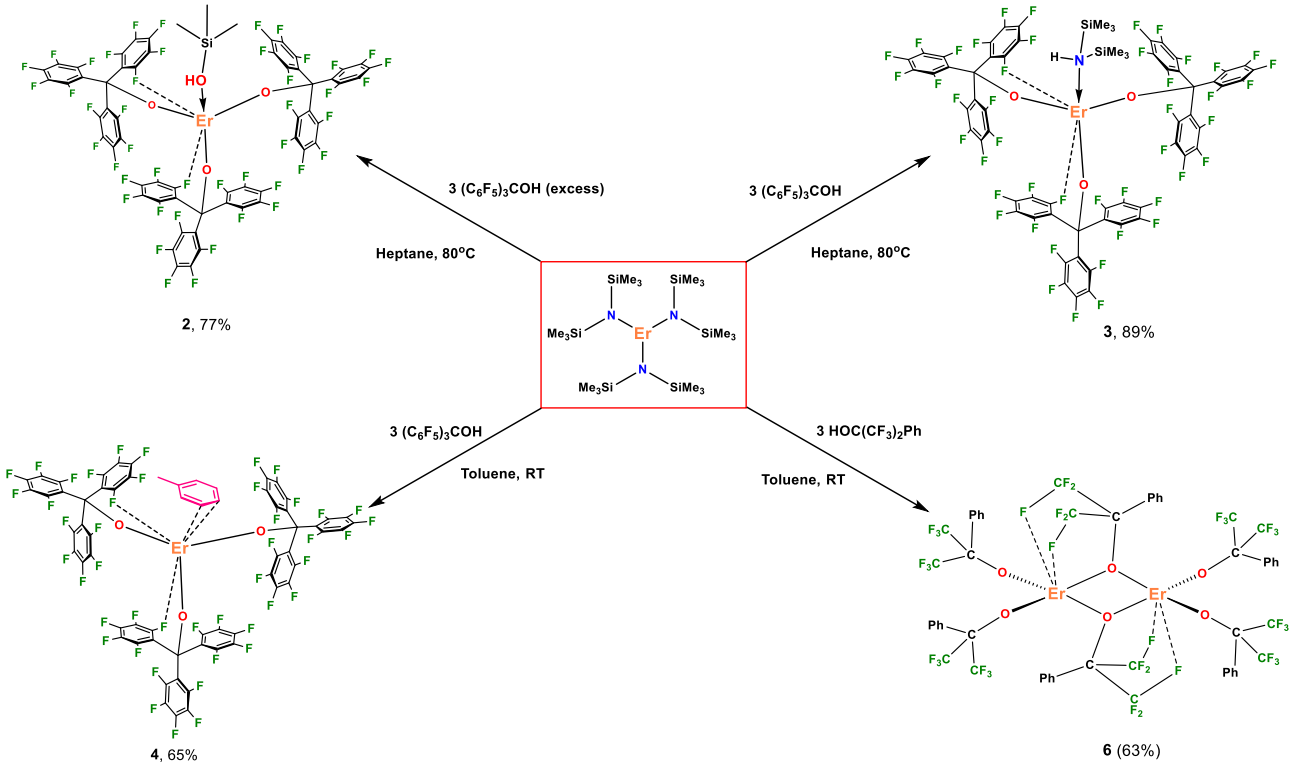

Scheme 2. Synthesis of complexes **2** - **4** and **6.**

distance is equal to 12.65 Å suggesting that dipolar interactions between the neighboring compounds are relatively weak.

The family of the related complexes **2**–**5** derived from fluorinated alkoxide $(C_6F_5)_3CO$ ligands in equatorial positions and one ligand in the axial position (Me_3SiOH (**2**), $(Me_3Si)_2NH$ (**3**), $C_6H_5CH_3$ (**4**) and *o*-$Me_2NC_6H_4CH_2$ (**5**)). However, due to the presence (or not) of the relatively closed Er···F contacts, these compounds present different geometry of the Er site. In compound **2**, Er^{3+} is coordinated by four oxygen atoms from three $(C_6F_5)_3CO$ and one $(Me_3Si)_2OH$ ligands making the Er site to also adopt a distorted trigonal pyramidal coordination geometry. Er^{3+} ion deviates from the plane consisting of the oxygen atoms of fluorinated alkoxides (0.73(2) Å) (Figure 1b). The Er–$O_{silanol}$ coordination bond of 2.380(8) Å is expectedly much longer than the covalent Er–$O_{alkoxides}$ bonds (2.034(2) Å). The three $O_{alkoxides}$–Er–$O_{alkoxides}$ angles are equal to 107.76(8)°, which is relatively close to the ideal trigonal planar angle of 113.4°. The O_{THF}–Er–$O_{alkoxide}$ angles lie in a wide range of 104.4(5)–122.7(3)° due to the disordering of the silanol group OH-fragment. The closest intermolecular Er···Er distance is equal to 11.24 Å suggesting that the complexes are relatively well isolated.

Another situation is observed in compounds **3** and **5**, where the Er^{3+} ion is surrounded by three oxygen atoms of three fluorinated alkoxides and a nitrogen from $(Me_3Si)_2NH$ or *o*-$Me_2NC_6H_4CH_2$ ligands, respectively, located in the axial position. The Er-O bond distances are equal to 2.071(3), 2.077(3) and 2.080(3) Å for **3** and 2.066(2), 2.082(2) and 2.083(2) Å for **5**. The Er–N bond length is of 2.522(4) and 2.49(2) Å for **3** and **5**, respectively. However, due to the presence of two short Er···F_{ortho} contacts (F atom in the *ortho*-position of the C_6H_5 ring of two fluorinated alkoxides) (2.632(2), 2.649(3) Å for **3** and 2.586(2), 2.615(2) Å for **5**), the geometry of Er site may be considered as distorted trigonal prism. The relevant angles are given in Table 1. Note that the structure of compound **5** is similar to the one previously reported for the aluminum complex $[(C_6F_5)_3CO]_3Al$.[67] Note also the occurrence of a relatively short contact (2.99(2) Å) between Er^{3+} and *ortho*-carbon of N,N-dimethyl-o-toluidine molecule in **5**. The closest intermolecular Er···Er distance is equal to respectively 11.38 and 12.03 Å for **3** and **5**, suggesting that the compounds are relatively well isolated and that dipolar interactions between the neighboring compounds are rather weak. In compound **4**, the Er^{3+} cation is surrounded by three fluorinated alkoxide ligands making three covalent bonds with erbium through oxygen atoms, and one toluene molecule (Figure 1d). It's important to note that according to the SC XRD data, Er^{3+} is disordered by two sites with the occupation ratio of 75% / 25%, respectively. In the first Er position (75%), toluene coordination is realized in η^3-fashion with the shorter Er···$C_{toluene}$ contacts of 2.75(2)–2.99(2) Å. The distances from Er^{3+} to other carbon atoms of the aromatic ring are much longer and vary within 3.32(2)–3.512(8) Å. In the second position (25%), the short Er···F_{ortho} contacts are detected with distances of 2.410(6), 2.550(7) and 2.593(5) Å. The latter are noticeably shorter than the ones observed in complexes **3** and **5**. Despite this, we do not take into account the short contacts Er···F when describing the coordination polyhedron in **4**, since they are observed only for 25% occupancy. Thus, the coordination polyhedron of Er^{3+} in **4** may be considered as distorted trigonal pyramid. Despite the disorder, the Er–O bond lengths are close to each other for both positions of Er^{3+} and lie in a rather narrow range of 1.990(6)-2.080(5) Å. The O–Er–O angles are in the range 112.3(2)–115.7(2)°. The closest intermolecular Er···Er distance of 10.41 Å is lower in comparison to what is observed for other compounds of this series indicating the possible occurrence of dipolar interactions.

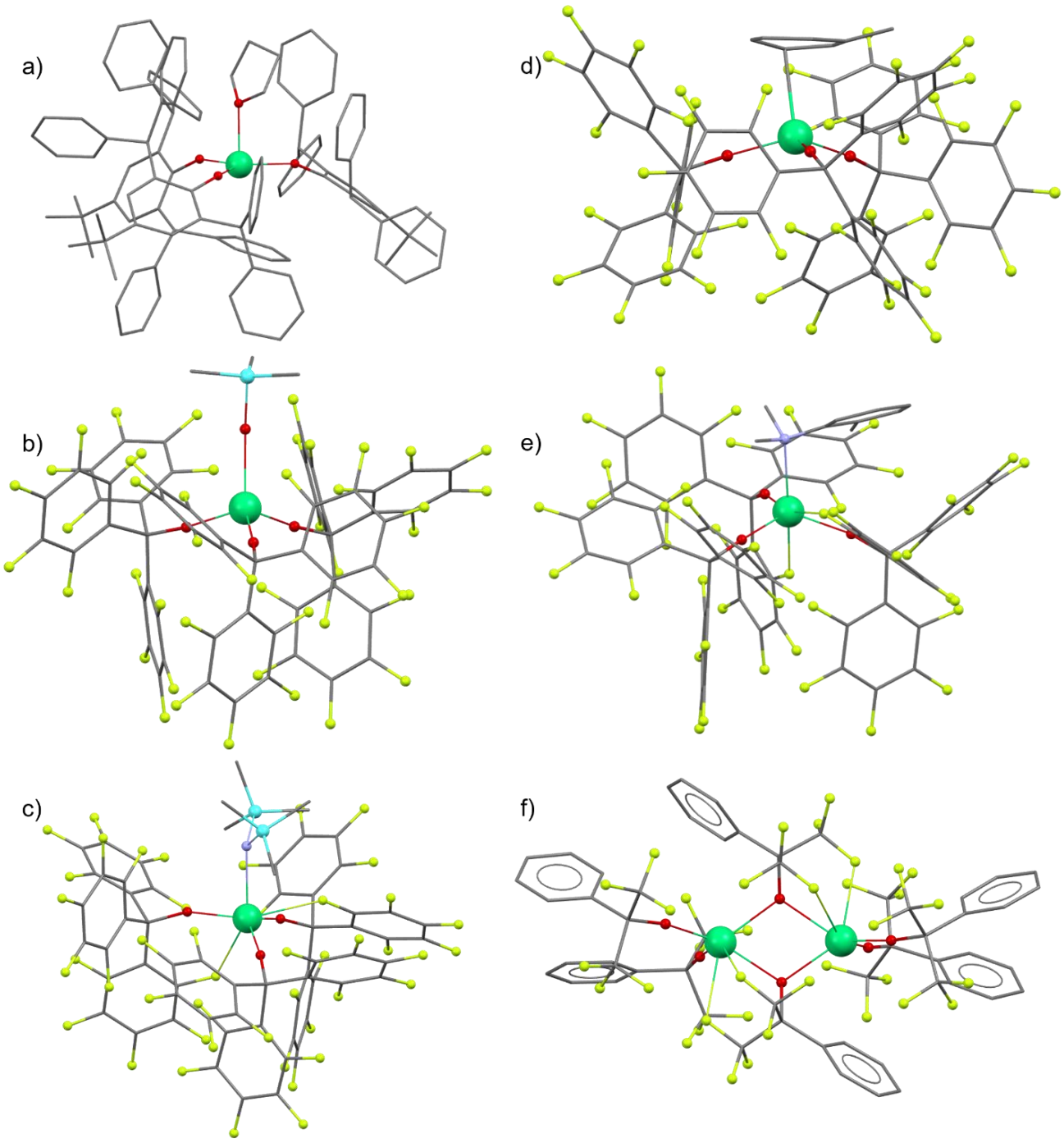

Figure 1. Molecular structures of compounds: a) **1**; b) **2**; c) **3**; d) **4**; e) **5**; f) **6**. All hydrogen atoms are omitted for clarity. Color codes: Er, green; C, grey; N, blue; O, red; Si, cyan.

A decrease in the ligand steric demand ([$Ph(CF_3)_2CO$ *vs* $(C_6F_5)_3CO$) results in the dinuclear structure of **6**. Two Er^{3+} ions are linked by two μ^2-O atoms of the bridging alkoxide ligands, additionally, each Er^{3+} ion exhibits two short contacts with F atoms of CF_3 groups. One Er···F contact is rather short (2.482(2), 2.514(2) Å), while the second one is noticeably longer (2.823(2), 2.825(2) Å). Thus, the coordination number of Er^{3+} ions in 6 is six and the geometry of the coordination environment of the metal centers can be described as a distorted trigonal prism. The Er–O bond lengths with terminal alkoxide ligands in 6 lie in the range 2.018(3)–2.049(3) Å and are slightly shorter than in related five-coordinate compound $[Ph(CF_3)_2CO]_3Er(OPPh_3)_2$ (2.07(2) Å).[26] Expectedly the Er–μ^2-O bonds for bridging alkoxide groups were found to be significantly longer (2.270(2)–2.303(2) Å) and only slightly shorter than the related distances in six-coordinate dimeric Er^{3+} alkoxide $\{[(CF_3)_2CHO]_2Er(OH_2)_2(\mu\text{-}OCH(CF_3)_2\}_2$ (2.288(4)–2.33(4) Å).[68]

Table 1. Main distances and angles for **1** – **6**.

Compound	Distance Er–O_{alkox} (Å)	Distance Er–X_{axial} (Å)	Distance Er···F (Å)	Angle O_{alkox}–Er–O_{alkox} (°)
1	2.082(2) 2.094(2) 2.086(2)	2.261(2)		118.01(5) 118.80(5) 123.16(5)
2	2.034(2)	2.380(8)	2.939(2)	107.77(8)
3	2.071(3) 2.077(3) 2.080(3)	2.522(4)	2.632(2) 2.649(3)	111.7(2) 122.4(2) 114.4(2)
4*	1.990(6) 2.003(5) 2.040(6)		2.410(6) 2.550(7) 2.593(7)	115.9(3) 120.9(2) 122.4(3)
5	2.066(2) 2.082(2) 2.083(2)	2.49(2)	2.586(2) 2.615(2)	111.9(2) 115.4(2) 120.9(2)
6**	2.018(3) 2.035(3) 2.036(2) 2.049(3)		2.482(2) 2.514(2) 2.823(2) 2.825(2)	 104.6(2) 106.3(2)

X_{axial} = donor atom in the axial position (O_{THF} for **1**, $O_{silanol}$ for **2**, N for **3**, **5**)
* data are given only for one position of the disordered cation
** data are given for terminal alkoxide ligands

Magnetic Properties

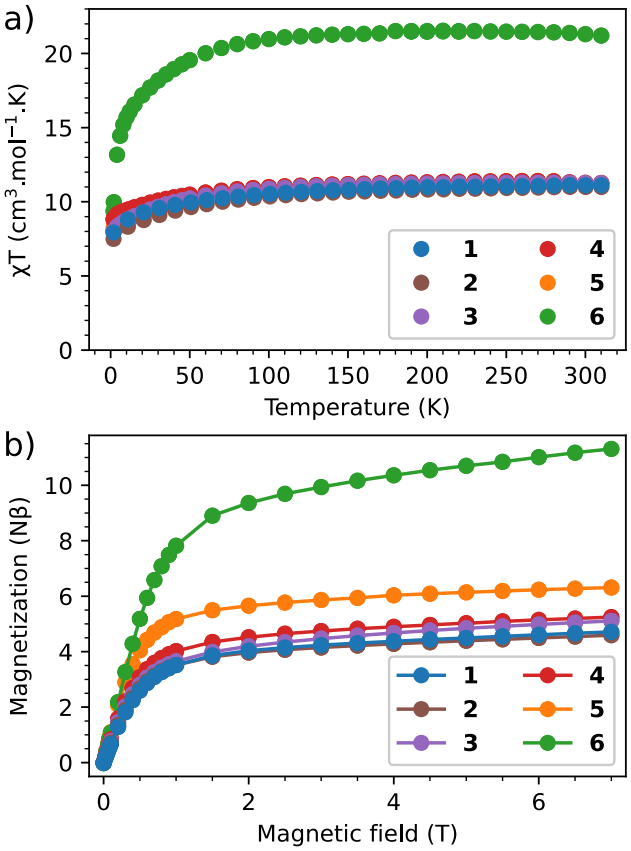

Figure 2. a) χT *vs* T curves performed under an applied magnetic field of 1000 Oe for **1**–**6**; b) Field dependence of the magnetization obtained at 1.8 K for **1**–**6**.

The magnetic properties of all compounds were investigated by using a SQUID MPMS3 magnetometer working between 1.8–350 K up to 7 T. The temperature dependences of the magnetic susceptibility performed in direct current (dc) mode were performed under an applied magnetic field of 1000 Oe. At room temperature, the χT values in $cm^3 \cdot mol^{-1} \cdot K$ obtained for **1**–**6** (11.1 for **1**, 11.0 for **2**, 11.3 for **3**, 11.3

$cm^3 \cdot mol^{-1} \cdot K$ for **4**, 11.3 $cm^3 \cdot mol^{-1} \cdot K$ for **5** and 21.5 $cm^3 \cdot mol^{-1} \cdot K$ for **6**) are in a good agreement with the expected theoretical for one isolated Er^{3+} center (J = 15/2, g = 1.2 with the expected χT value of 11.48 $emu \cdot mol^{-1} \cdot K$) for **1**–**5** or two isolated Er^{3+} ions for **6** (the expected χT value of 22.96 $emu \cdot mol^{-1} \cdot K$). Decrease of the temperature induces the gradual decrease of the χT product, which reflects the conventional thermal depopulation of the m_J levels (Figure 2a) in **1**–**5** and along with possible antiferromagnetic interactions between Er^{3+} for **6**.
The field dependences of the magnetization performed at 1.8 K show a rapid increase of the magnetization in the low field region and then its slow increase after 1T (Figure 2b). The saturation of the magnetization is never reached event up to 7 T indicating the presence of a significant magnetic anisotropy, as usually observed in lanthanide-based complexes.

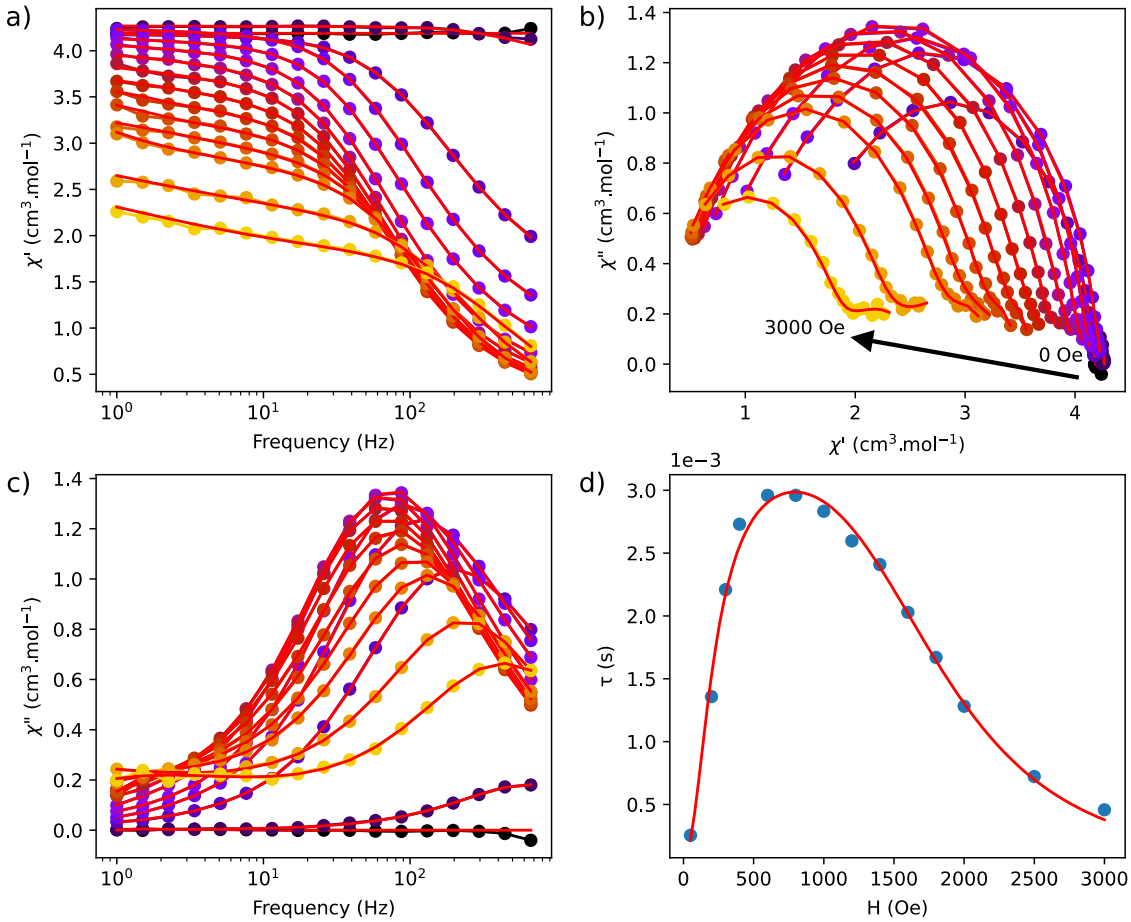

Figure 3. Frequency dependence of χ' (a) and χ'' (c) for **1** at 1.8 K performed under various applied dc fields. (b) Cole-Cole plots obtained using the frequency dependence of χ'' for **1** at 1.8 K under various dc field. The solid lines correspond to the best fit obtained with a generalized Debye model. (d) Field dependence of the relaxation time for **1**. The red line represents the fit using Eq. (1).

The dynamic behavior in the alternating current (ac) mode performed for compounds **1**–**6** was investigated at low temperature in the aim to explore the occurrence of a slow relaxation of the magnetization. No significant signal of out-of-phase (χ'') components of the ac susceptibility was observed for 1–6 in zero dc magnetic field. Then, the frequency dependence of the ac susceptibility was investigated in the presence of different applied dc magnetic fields in order to suppress the eventual Quantum Tunneling of Magnetization (QTM) process. The detailed description of the dynamic properties is given for compound 1 in the main text and in ESI for other compounds (Figures S7–S16). The main magnetic parameters are gathered in Table 2.
A series of frequency dependent pics of χ' and χ'' components of the ac susceptibility was obtained under different applied dc fields for 1 indicating that the QTM process can be efficiently suppressed (Figures 3a, 3c). The corresponding Cole-Cole plot fitted with a generalized Debye model can be seen in Figure 3b. The field dependence of the relaxation time presents a clear maximum. This curve was fitted with Eq. (1) in order to determine the optimal magnetic field to apply (Figure 3d):

$$\boldsymbol{\tau^{-1} = D \cdot H^2 \cdot T + \frac{B_1}{1 + B_2 \cdot H^2} + C} \qquad (1),$$

where the first term accounts for the direct relaxation process (for Kramers-ion), the second for the QTM and the third for relaxations which are not dependent of the field (Orbach and Raman relaxations). For the specific case of $B_2 \times H^2 >> 1$, then the QTM term of Eq. (1) can be rewritten as B_0/H^2. The experimental points are well fitted by Eq. (1) (red line of the curve) and the fit's values can be found in Table S3. The maximum value of the relaxation time, which determine the optimal applied magnetic field, is 800 Oe. For this reason, this value was chosen for further temperature-dependent experiments.

The frequency dependence of the in-phase (χ') and the out-of-phase (χ'') components of the ac susceptibility performed under 800 Oe are shown on Figures 4a and 4c, respectively. A single frequency dependent peak, which shifts towards higher frequency as the temperature increases (from 1.8 to 2.9 K) can clearly be seen for χ''. The corresponding Cole-Cole plots fitted with a generalized Debye model, gave moderate α parameter values (between 0.1 and 0.25) indicating a certain distribution of the relaxation times (Figure 4b). The temperature dependence of the relaxation time was fitted by using Eq. (2):

$$\boldsymbol{\tau^{-1} = \tau_0^{-1} \cdot exp\left(-\frac{U_{eff}}{k_B T}\right) + A + B \cdot T^n} \quad (2),$$

where the first term accounts for the Orbach process, the second term accounts for the QTM process, and the last term accounts for the Raman process (with n ranging from 2–9). For sample **1**, the value of the n parameter is 3. Figure 4d illustrates the optimum fit that can be obtained using Eq. (2). The optimized parameters are: U_{eff} = 34.3±0.5 K, τ_0 = (9±4)×10^{-9} s, B = 135±1 s^{-1}·K^{-3} and A is neglected. These parameters indicate that in **1**, Raman process is rather dominant beside the Orbach relaxation, while QTM has been efficiently suppressed by an application of the magnetic field.

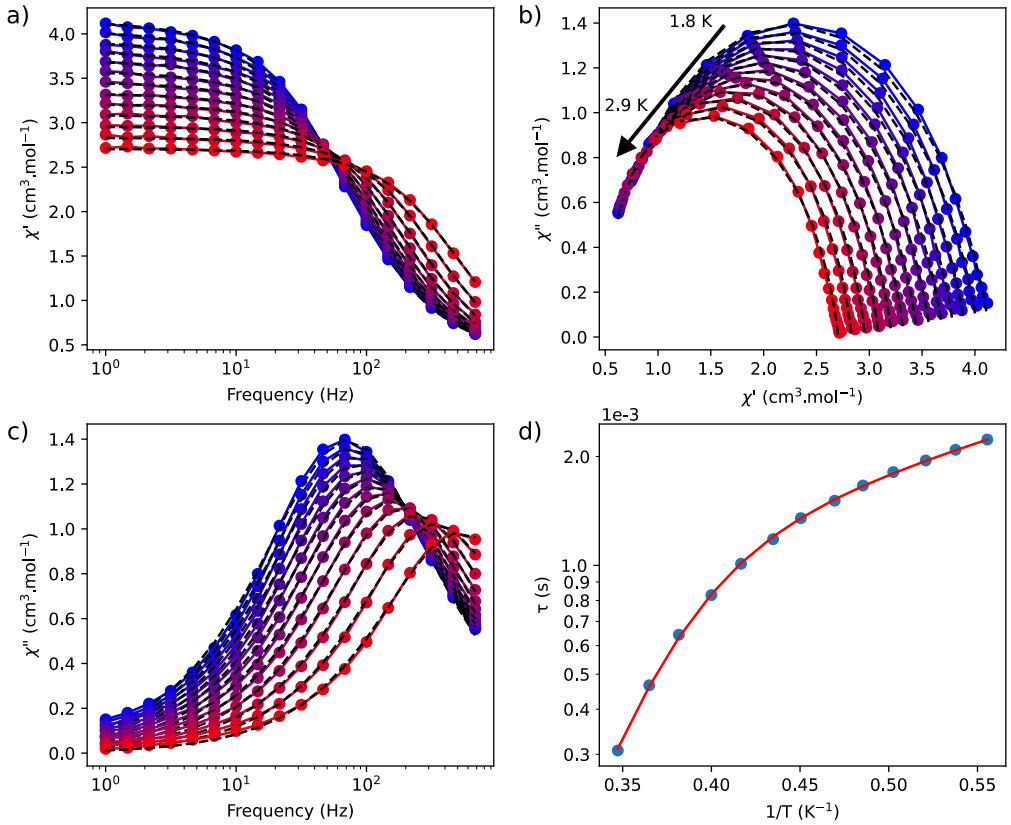

Figure 4. Frequency dependence of the in-phase, χ', (a) and out-of-phase, χ" (c) components of the ac susceptibility for **1** under optimal applied magnetic field of 800 Oe. The red lines are the result of the Cole-Cole fitting. (b) Cole-Cole plots obtained using the frequency dependence of χ" for **1** obtained under 800 Oe. The solid lines correspond to the best fit obtained with a generalized Debye model. (d) Temperature dependence of the relaxation time for **1** (800 Oe) and the corresponding fit with Eq. (2) (red solid line).

Dynamic properties of compounds **2** and **4** also having the trigonal pyramidal geometry of the Er site, but presenting longer distance between Er^{3+} and the donor atom located in the axial position (2.380 for **2** and 2.754 for **4** *vs* 2.290 Å for **1**), have been investigated in the same manner (Figure S7, Figure S8, ESI). The fitting with Eq. (2) of the temperature dependence of the relaxation time performed under optimum magnetic field of 1000 Oe permitted to determine the following parameters (Figure 5, Table 2): U_{eff} = 26.0±1 K, τ_0 = (1.0±0.3)×10^{-6} s, A = 57±3 s^{-1} (B is neglected) for **2** and U_{eff} = 24.7±0.3 K, τ_0 = (2.7±0.2)×10^{-5} s, A = 5.5±0.1 s^{-1} and B = (2.9±0.1)×10^{-3} s^{-1}·K^{-7} for **4**. Note that both ln(τ) *vs* T^{-1} curves show a transition from a thermally activated to a temperature independent regime below 2.5 K (Figure 5). These parameters indicate that the QTM process is still present for both of them, while Raman relaxation can rather be neglected in **2**.

Dynamic properties of compounds **3**, **5** and **6** presenting rather distorted trigonal prismatic geometries of the Er sites were also investigated in details and the results are shown in Figures S9–S16 (ESI), Figure 5, Table 2. All of them present field induced SMM behaviors with the effective energy barriers comprised between 20 and 30 K. In comparison to compounds **1**, **2**, **4** and **6**, which present only one relaxation mechanism, samples **3** and **5** show a double magnetic relaxation. Several relaxations have commonly been attributed to the various environments of the lanthanide ion, including distinct crystallographic locations in a polynuclear cluster or coordination ligand disorders, which is not the case of samples **3** and **5**. Surprisingly, compound **4** exhibiting an important disorder of Er site displays only one magnetic relaxation. Alternatively, the occurrence of two relaxation processes could be explained by the distribution of the energy levels in the lanthanide system, forming a double well pattern. Quantum tunneling can occur between different levels, and the application of a very small field may promote or hinder such tunneling, thereby slightly altering the energy level match or mismatch.[48] Figure 5 displays the temperature

dependences of the magnetic relaxation times for samples **1**–**6** with the main parameters summarized in Table 2. The analysis of the obtained parameters suggests that the expected decreasing of the Raman relaxation through the use of fluorinated alkoxides occurred for tetranuclear compounds **2** and **6**, in comparison with **1** involving non fluorinated ligands. However, this situation is not confirmed for samples **3**–**5** (with coordination numbers >4), for which the Raman relaxation is dominant despite the presence of fluorinated ligands.

Table 2. Main magnetic parameters for **1** – **6**.

Compound	U_{eff}, K	τ_0, s	n	A, s^{-1}	B, $s^{-1}.K^{-n}$
1	34.3±0.5	$(9.0\pm4.0)\times10^{-9}$	3	–	135±1
2	26±1	$(1.0\pm0.3)\times10^{-6}$	–	57±3	–
3	28.4±0.2	$(1.29\pm0.6)\times10^{-6}$	–	6.3±1.0	–
	-	-	3	51±15	23.1±0.5
4	-	-	7	6.5±1.4	$(5.6\pm0.2)\times10^{-3}$
5	–	–	7	8.2±0.9	0.1294±0.0003
	-	-	3	–	72.4±2.5
6	21.8±0.4	$(4.1\pm0.5)\times10^{-6}$	–	5.2±0.4	–

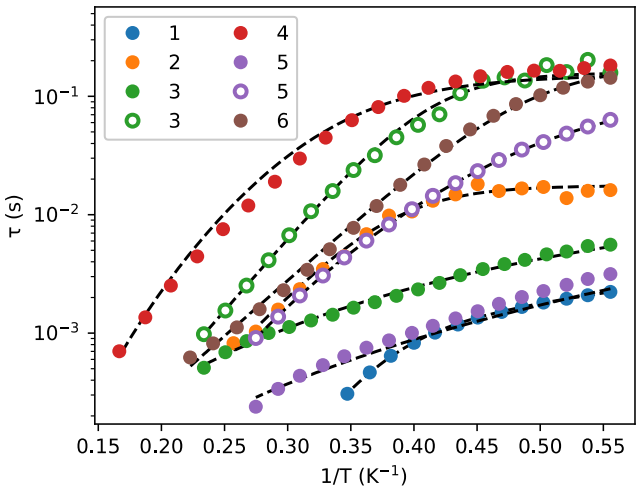

Figure 5. Temperature dependence of the relaxation time for samples **1**-**6** and the corresponding fits with Eq. (2) (black dashed lines). Open symbols represent the second relaxation time when it occurs.

Photoluminescence investigations

The photoluminescence of compounds **1**–**6** was investigated in solid state at 77 K and at room temperature (300 K) (Figure 6). In the excitation spectra of complexes **1**–**4** and **6**, a large intense band is observed in the range 300–450 nm, which can be associated with sensitizing luminescence through electronic transitions within the ligand environment so-called "antenna effect". In addition, excitation spectra of complexes **1**–**4** show narrow bands corresponding to the direct excitation of the Er^{3+} ion *via* the $^4I_{15/2}\rightarrow{}^4G_{11/2}$ and $^4I_{15/2}\rightarrow{}^2H_{11/2}$ transitions. Finally, for complex **6**, additional transitions $^4I_{15/2}\rightarrow{}^2H_{9/2}$, $^4I_{15/2}\rightarrow{}^2F_{3/2}+{}^2F_{5/2}$ and $^4I_{15/2}\rightarrow{}^2F_{7/2}$ can be detected.[69] In contrast, in the spectrum of complex **5**, only weakly intense bands associated with the direct excitation of the Er^{3+} ion are observed. Such behavior in the optical excitation of complex **5** indicates a weak transfer of electronic excitation energy from the

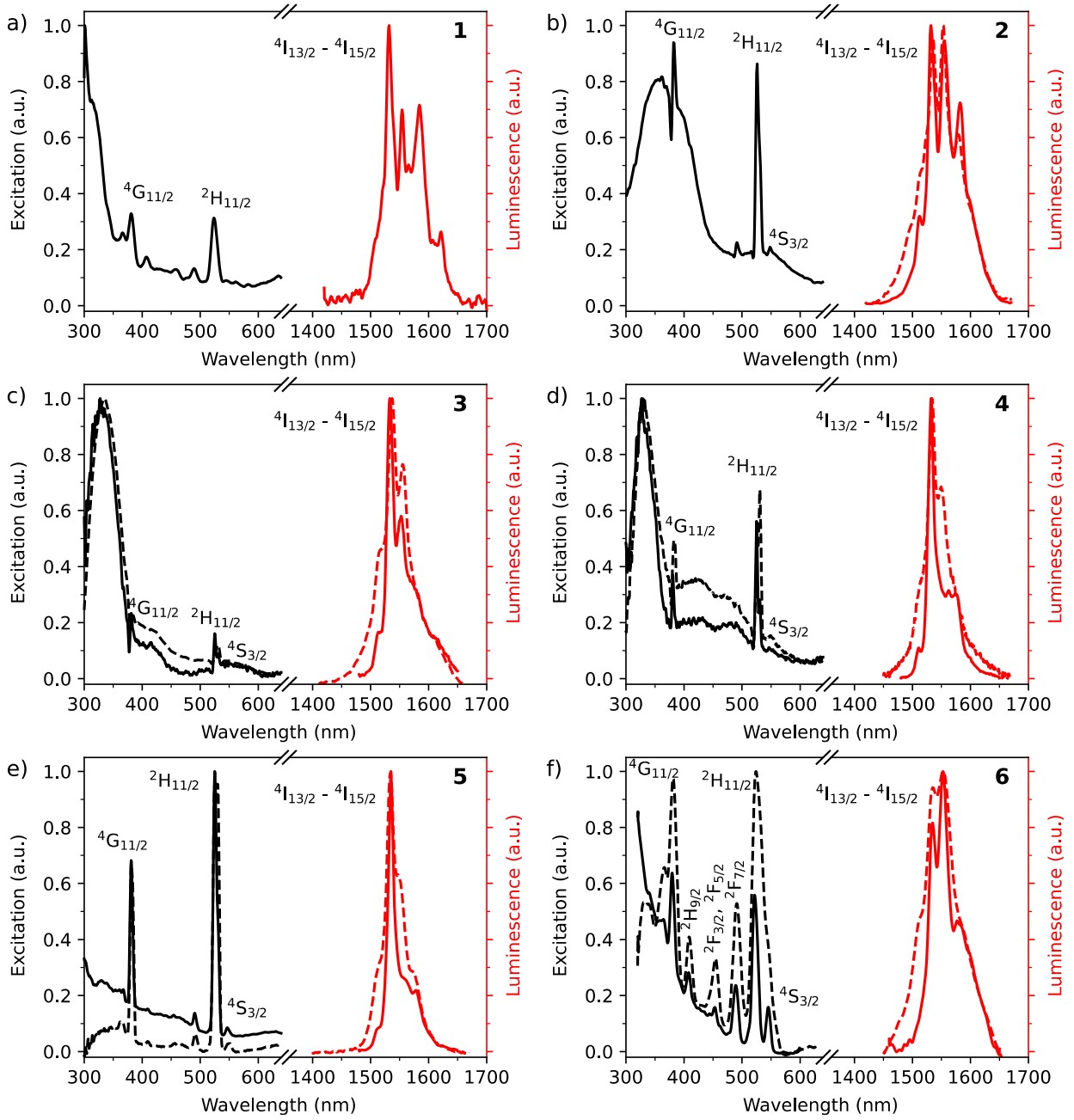

Figure 6. Spectra of optical excitation at 360 nm (black curves) and emission (red curves) for compounds **1**–**6** (a to f, respectively) at temperatures of 300 K (dashed lines) and 77 K (plain lines).

donor ligand to the acceptor Er^{3+} ion (antenna effect is not operational).

When optically excited in a wide spectral range from 280 to 700 nm, an emission is observed solely in the NIR telecommunication range with a pronounced local maximum at ~1540 nm at 77 K for all complexes **1**–**6**, while at room temperature the emission is operational for compounds 2–6 (Figure 6). No noticeable changes in the emission spectra shape were observed depending on excitation wavelength. These emission bands are attributed to the f*–f transition of the $^4I_{13/2} \rightarrow {}^4I_{15/2}$ within the Er^{3+} ion.[70] Note also that there are no contributions associated with the fluorescence or phosphorescence of the ligand environment in the luminescence spectra of all complexes. This observation indirectly confirms the relatively efficient energy transfer from the electronically excited donor ligand to the acceptor ion.

The emission decay curves of compounds **1**–**6** were monitored in solid state at 77 and 300 K within the $^4I_{13/2} \rightarrow {}^4I_{15/2}$ transition. In the simplest case, luminescence kinetics can be explained by a two-level model, where relaxation occurs strictly from one excited state, and it follows a mono-exponential law:

$$\mathbf{I(t) = I_0 exp\,(-t/t_{obs})} \quad (3),$$

where the observed decay time

$$\mathbf{t_{obs} = \frac{1}{k_{obs}} = \frac{1}{k_{rad} + k_{nrad}}} \quad (4)$$

is determined by two rate constants, k_{rad} for radiative relaxation and k_{nrad} for non-radiative relaxation, respectively. The luminescence kinetics of complex 4 in the solid phase at temperatures of 77 K and 300 K, when optically excited through the ligand environment (at 360 nm), are depicted in Figure S26, (ESI). For complexes 2–5, the behavior of luminescence kinetic profiles exhibits similar nature. It was not possible to record the luminescence kinetics for samples 1 and 6 (the luminescence decay times of these samples are significantly shorter than the instrument's characteristic time for the IRF function). The luminescence kinetics of complexes **2**–**5** were fitted with a mono-exponential function, which confirms the presence of a single type of emitting centers. The calculated luminescence decay times (t_{obs}) in such cases range from 23 to 73 μs Table 3. The maximum decay time of 73 μs is obtained for complex 4 when excited at a wavelength of 360 nm at a temperature of 77 K. Note that such a long lifetime is rare for luminescent Er^{3+} SMM (Table S1).

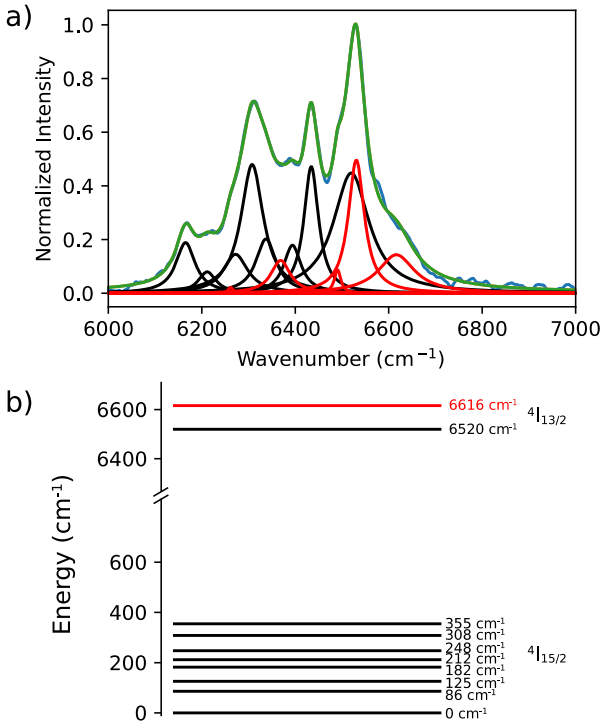

Fig. 7. a) Luminescence emission spectrum for crystalline complexes **1** at 77 K. The blue and green curves represent the experimental data and the optimized fit. The black and red Lorentzian functions represent the radiative relaxation from the first and second $^4I_{13/2}$ states, respectively. b) Schematic representation of the energy levels for sample **1**, extracted from the fitting process.

Magneto-optical correlation

In order to exploit the luminescent properties of Er^{3+} as an experimental probe for the crystal field splitting of the M_J sublevels of Er^{3+} in these complexes, the NIR emission spectra were fitted with multi- Lorentzian functions. For this purpose, two first states of $^4I_{13/2}$ and the eighth states of $^4I_{15/2}$ were used. The energy levels were simultaneously optimized for the spectra taken at both 77 and 300 K, ensuring that the energy levels for a given sample remain constant irrespective of temperature. The areas under the Lorentzian function derived from the $^4I_{13/2}$ → $^4I_{15/2}$ transitions have been maintained unchanged. A temperature coefficient was only added to the 300 K spectrum to account for luminescence quenching and changes in the populations of $^4I_{13/2}$ due to Boltzmann statistics. The $^4I_{15/2}$ level exhibit a maximum Stark splitting of eight. The occurrence of additional transitions possibly stems from hot bands like the emission from the first excited Stark levels of the $^4I_{13/2}$ multiplet. Assigning these transitions allows us to delineate the energy diagram of the Stark sub-levels and correlate them with the magnetic measurements (Figure 7 for **1** and Figures S24–S28 (ESI) for **2**–**6**). The energy gaps (⍰E) between the ground and the first excited state of the $^4I_{15/2}$ crystal field splitting for all compounds are gathered in Table 3 and compared with the U_{eff} values obtained by dynamic magnetic measurements. In all cases the magnetic measurements provide the effective energy barriers, which are underestimated in comparison with the experimental ΔE values obtained from photoluminescence Table 3. This can be explained by the dominant Raman relaxation processes for **1**, **4** and **5** along with the QTM, which highly impact the magnetism. Note that these examples are the second examples of Er^{3+}-based SMMs demonstrating an experimental magneto-luminescent correlation.

Table 3. Luminescence parameters for **1–6** and magneto-optical correlation.

Compound	λ, nm	T, K	t_{obs}, μs	ΔE[a], cm^{-1}	U_{eff}[b], cm^{-1}
1	–	–	–	86	24
2	360	300	23±1	37	18
		77	23±1		
3	360	300	35±1	92	20 and 4
		77	35±1		
4	360	300	71±1	40	17
		77	73±2		
5	360	300	64±1	43	5
		77	62±2		
6	–	–	–	84	15

Taking into account that the radiative lifetime (τ_{rad}) of Er^{3+} ranges 2-3 μs, the quantum efficiency (η) of these compounds is $\eta = t_{obs}/t_{rad} \approx 3\%$;
[a]ΔE is the energy gaps between the ground and the first excited state of the $^4I_{15/2}$ crystal field splitting experimentally determined form the luminescence;
[b]U_{eff} is the effective energy barrier determined by dynamic magnetic measurements.

Experimental

General Procedure

All operations were carried out under an atmosphere of argon using Schlenk techniques or in nitrogen filled glovebox. After drying over KOH, THF was purified by distillation from sodium/benzophenone ketyl. Hexane, heptane and toluene were dried over Na/K alloy, transferred under vacuum, and stored in the glovebox. Fluorinated alcohol $Ph(CF_3)_2COH$ was purchased from SIA "P&M-Invest" Ltd, was dried over molecular sieves, then condensed in vacuum prior to use. $Er[N(SiMe_3)_2]_3$ and $Er(o\text{-}NMe_2C_6H_4CH_2)_3$ were synthesized according to the literature procedures.[71,72] 4-*t*Bu-2,6-$(Ph_2CH)_2C_6H_2OH$ and $(C_6F_5)_3COH$ were synthesized according to the literature procedures.[73,74] The C, H, N elemental analyses were carried out in the microanalytical laboratory of IOMC by means of a Carlo Erba Model 1106 elemental analyzer with an accepted tolerance of 0.4 unit on carbon (C), hydrogen (H), and nitrogen (N). Lanthanide analysis was carried out by complexometric titration.[75] IR spectra were recorded as Nujol mulls on a Bruker-Vertex 70 spectrophotometer.

Synthesis of [4-*t*Bu-2,6-$(Ph_2CH)_2C_6H_2O]_3Er(THF)$ (1): 4-*t*Bu-2,6-$(Ph_2CH)_2C_6H_2OH$ (1.26 g, 2.63 mmol) was added to a yellow solution of $(o\text{-}Me_2NC_6H_4CH_2)_3Er$ (0.50 g, 0.88 mmol) in THF (10 mL) under stirring. The solution instantly changed color to pink and was stirred for another 2 h at room temperature, then all volatiles were removed in vacuo. The resulting foamy residue was redissolved in toluene (3 mL). Pink crystals of 1 were obtained by slow diffusion of hexane into a toluene solution (75%, 1.10 g). Elemental analysis calcd. (%) for $C_{60}H_{10}ErF_{45}O_4Si$ (1845.01 g·mol^{-1}): C, 39.06; H, 0.55; Er, 9.07; found C, 39.34; H, 0.47; Er, 9.20. IR (Nujol, KBr) ν·cm^{-1}: 1951 (w), 1889 (w), 1806 (w), 1599 (s), 1493 (s), 1298 (s), 1184 (s), 1155 (w), 1119 (m), 1076 (m), 1026 (s), 912 (m), 893 (m), 868 (s), 847 (s), 766 (s), 702 (s), 680 (m), 623 (s), 605 (s), 567 (s), 538 (m).

Synthesis of $[(C_6F_5)_3CO]_3Er(Me_3SiOH)$ (2): A five-fold molar excess of $(C_6F_5)_3COH$ (0.87 g, 1.65 mmol) was added to a pink solution of $[(Me_3Si)_2N]_3Er$ (0.22 g, 0.33 mmol) in heptane (10 mL) under vigorous stirring. The reaction mixture was stirred for additional 2 h and a fine crystalline pink powder precipitated. Pink crystals of 2 were obtained by slow cooling of a hot saturated solution in heptane (77% yield, 0.47 g). Elemental analysis calcd. (%) for $C_{60}H_{10}ErF_{45}O_4Si$ (1845.01 g·mol^{-1}): C, 39.06; H, 0.55; Er, 9.07; found C, 38.74; H, 0.47; Er, 9.20. IR (Nujol, KBr) ν·cm^{-1}: 3317-3267 (s, SiOH), 1653 (s), 1590 (w), 1528 (s), 1302 (s), 1264 (s), 1130 (s), 1026 (s), 989 (s), 868 (m), 843 (s), 795 (s), 766 (m), 750 (m), 698 (s), 667 (m), 642 (s), 619 (m), 571 (s).

Synthesis of $[(C_6F_5)_3CO]_3Er[(Me_3Si)_2NH]$ (3): $(C_6F_5)_3COH$ (0.53 g, 1.00 mmol) was added to a pink solution of $[(Me_3Si)_2N]_3Er$ (0.22 g, 0.33 mmol) in heptane (10 mL) under vigorous stirring. After 1 h a fine crystalline precipitate of complex 3 formed (0.56 g, 89%). Pink crystals of 3 suitable for X-ray analysis were obtained by slow cooling of a boiling saturated solution of the complex in heptane to room temperature. Elemental analysis calcd. (%) for $C_{63}H_{19}ErF_{45}NO_3Si_2$ (1916.21 g·mol^{-1}): C, 39.49; H, 1.00; N, 0.73; Er, 8.73; found C, 39.16; H, 0.87; N, 0.80; Er, 8.88. IR (Nujol, KBr) ν·cm^{-1}: 3502-3184 (s, NH), 1653 (s), 1528 (s), 1399 (m), 1304 (s), 1262 (s), 1125 (s), 1024 (s), 1007 (s), 974 (s), 864 (s), 845 (s), 795 (s), 767 (m), 750 (m), 700 (s), 667 (m), 640 (m), 619 (m), 567 (s).

Synthesis of $[(C_6F_5)_3CO]_3Er(C_6H_5CH_3)$ (4): $(C_6F_5)_3COH$ (0.53 g, 1.00 mmol) was added to a pink solution of $[(Me_3Si)_2N]_3Er$ (0.22 g, 0.33 mmol) in hexane (10 mL) under vigorous stirring. The solution was stirred for additional 2 h and a fine crystalline pink powder precipitated. The volatiles were removed in vacuo and the solid residue was redissolved in toluene (3 mL). Pink crystals of 4 were obtained by slow diffusion

of hexane (15 mL) into toluene solution (0.39 g, 65%). Elemental analysis calcd. (%) for $C_{64}H_8ErF_{45}O_3$ (1846.95 g·mol^{-1}): C, 41.62; H, 0.44; Er, 9.06; found C, 41.38; H, 0.37; Er, 9.34. IR (Nujol, KBr) ν·cm^{-1}: 1653 (s), 1526 (s), 1300 (s), 1264 (w), 1211 (w), 1123 (s), 1022 (s), 1005 (s), 991 (s), 978 (s), 864 (m), 845 (m), 798 (s), 767 (m), 747 (m), 700 (s), 665 (w), 638 (w), 621 (w), 571 (s).

Synthesis of [$(C_6F_5)_3CO]_3Er(o$-$Me_2NC_6H_4CH_3$) (5): $(C_6F_5)_3COH$ (0.53 g, 1.00 mmol) was added to a yellow solution of (o-$Me_2NC_6H_4CH_2)_3Er$ (0.19 g, 0.33 mmol) in toluene (10 mL) under vigorous stirring. In 10 min the solution turned pink and the reaction mixture was stirred for another 1 h. The resulting solution was concentrated to 2 mL. Large pink crystals of 5, suitable for X-ray analysis were obtained by slow diffusion of hexane (15 mL) into the toluene solution of 5 (0.54 g, 87%). Complex 5 crystallizes as a solvate with one molecule of toluene. Elemental analysis calcd. (%) for $C_{66}H_{13}ErF_{45}NO_3$ (1890.02 g·mol^{-1}): C, 41.94; H, 0.69; N, 0.74; Er, 8.85; found C, 42.25; H, 0.73; N, 0.70; Er, 8.88. IR (Nujol, KBr) ν·cm^{-1}: 1653 (s), 1527 (s), 1301 (s), 1264 (w), 1245 (w), 1210 (w), 1125 (s), 1015 (s), 1005 (s), 991 (s), 978 (s), 864 (m), 845 (m), 840 (m), 798 (s), 767 (m), 747 (m), 700 (s), 665 (w), 631 (w), 620 (w), 570 (s).

Synthesis of {[Ph($F_3C)_2CO]_2Er[\mu^2$-$OC(CF_3)_2Ph]\}_2$ (6): A solution of $Ph(CF_3)_2COH$ (0.26 g, 1.06 mmol) in toluene (10 mL) was added to a solution of $Er[N(SiMe_3)_2]_3$ (0.325 g, 0.50 mmol) in toluene (10 mL) at ambient temperature. The solution was stirred for 30 min. The volatiles were removed in vacuo. The oily residue was dried in vacuo at 50 °C for 30 min and then was dissolved in fresh portion of toluene (approx. 5 mL). Cooling of the resulted solution at −30 °C for 24 h afforded pink crystals of 6. The mother liquid was decanted and the crystals were dried in vacuo for 30 min. Complex 6 was isolated in 63% yield (0.285 g). Elemental analysis calculated for $C_{54}H_{30}Er_2F_{36}O_6$ (1793.27 g·mol^{-1}): C, 36.17; H, 1.69; Er, 18.65. Found: C, 35.95; H, 1.53; Er, 18.52. IR (Nujol, KBr) ν·cm^{-1}: 1955 (m), 1885 (m), 1810 (m), 1690 (m), 1605 (m), 1585 (m), 1500 (s), 1270 (s), 1215 (s), 1075 (s), 1035 (m), 970 (s), 940 (s), 920 (s), 760 (s), 695 (m), 655 (w), 555 (s), 535 (s), 500 (s), 480 (m).

X-ray crystallography.

The single crystal X-ray diffraction (SC XRD) data for **1**-**6** were collected at 100.0(2) K with a *Bruker D8 Quest* diffractometer using graphite monochromated $Mo_{K\alpha}$ radiation (λ = 0.71073 Å, ω-scans). Structures were solved *via* intrinsic phasing algorithm with the XT[76] structure solution package in Olex2[77] and then refined with the XL[78] refinement package using least-squares minimization against F^2 in the anisotropic approximation for non-hydrogen atoms. The hydrogen atoms of the OH group in **2** and of the NH group in **3** were located from difference Fourier synthesis, positions of other hydrogen atoms were calculated, and they all were refined in the isotropic approximation within the riding model. Disordered lattice molecules of hexane in **3** and of toluene in **4** and **5** were treated as diffuse contributions to the overall scattering without specific atom positions using the solvent mask routine implemented in Olex2. Crystal data and structure refinement parameters are given in Table S2. CCDC 2294568 (**1**), 2291007 (**2**), 2291005 (**3**), 2291008 (**4**), 2291006 (**5**), and 2291004 (**6**) contain the supplementary crystallographic data for this paper.

Photoluminescence spectra

Spectra of optical excitation and luminescence in the visible and NIR regions were recorded using the Fluorolog QM spectrofluorometer, operating in the range of wavelengths from 300 to 1700 nm. Measurements were performed at room temperature (300 K) for crystalline and powdered samples enclosed in sealed quartz capillaries. For low-temperature measurements, powdered samples were cooled to 77 K using a nitrogen-cooled quartz cryostat. A xenon arc lamp, included in the Fluorolog QM setup, served as the continuous excitation source. This spectrofluorometer was also used to record the time-dependent intensity of luminescence during pulsed optical excitation. For microsecond time resolution, an impulse xenon lamp, also part of the spectrofluorometer, with a pulse duration of 50 µs and an upper pulse repetition frequency limit of 300 Hz was used.

The photoluminescence spectra were fitted using the least-squares method and Lorentzian functions. For samples **2**–**6**, both the 77 K and 300 K spectra were utilized to perform the fit, while only the 77 K spectrum was used for sample **1** (no detection of luminescence at room temperature). The energy levels have been optimized simultaneously for the 77 K and 300 K spectra so that the energy levels for a given sample remain constant regardless of temperature. In this analysis, we utilized the two first states of $^4I_{13/2}$ and the eighth states of $^4I_{15/2}$. The Lorentzian function's areas derived from $^4I_{13/2} \rightarrow {}^4I_{15/2}$ transitions were kept constant at both temperatures. A temperature coefficient was only added to the 300 K spectrum to account for luminescence quenching and changes in the populations of $^4I_{13/2}$ due to Boltzmann statistics.

Magnetic measurements

Magnetic measurements were performed using a Quantum Design MPMS-XL SQUID magnetometer working between 1.8–350 K with the magnetic field up to 7 Tesla. The samples were prepared in glovebox. The data were corrected for the sample holder and the diamagnetic contributions calculated from the Pascal's constants.

Conclusions

In summary, in this article we reported a new series of luminescent Er^{3+}-based field induced SMMs obtained by using a combination of phenolate or fluorinated alkoxide ligands with different complementary ligands (THF, Me_3SiOH, $(Me_3Si)_2NH$, $C_6H_5CH_3$, *o*-$Me_2NC_6H_4CH_2$) located in the axial position in order to explore the potential of four-coordinated Er^{3+} geometry in luminescent SMMs. The use of fluorinated alkoxides has been motivated by several reasons: (*i*) suppression of non-radiative deactivation process in the aim to improve the Er^{3+} based luminescence, (*ii*) decreasing the Raman relaxation through the possible formation of more rigid structures, (*iii*) steric and coordination saturation of Er center, in order to stabilize the low coordination Er^{3+} complexes in the aim to reinforce the crystal field in the equatorial position of Er^{3+} ion. By using this strategy, we synthesized three four-coordinate complexes (**1**, **2** and **4**) in which Er^{3+} ion is truly four-coordinated and adopts distorted trigonal pyramidal geometry with rather long distance between Er^{3+} and the donor atom of ligands located in the axial position. However, compounds **3** and **5** may be considered as six-coordinate because the fluorinated alkoxide ligands form the relatively close Er···F contacts. Compound **6** presents dinuclear structure in which each Er site is also 6-coordinate. All investigated compounds exhibit a slow relaxation of

the magnetization under an applied static magnetic field thanks to suppressing/decreasing of the QTM process. Note that the strategy dealing with the use fluorinated alkoxides to decrease the Raman relaxation seems to work in the case of compounds **2** and **6**. Secondly, all compounds display a characteristic NIR emission attributed to the $^4I_{13/2} \rightarrow {}^4I_{15/2}$ transition of Er^{3+} making them multifunctional luminescent SMMs. The excitations were obtained through an antenna effect, indicating that, as anticipated, the phenolate or fluorinated alkoxide ligands effectively work sensitizing Er^{3+}. Notably, these compounds exhibit an impressive extended lifetime, reaching up to 73 μs, which is rather rare for luminescent SMMs. The emission spectra of all compounds were exploited to establish the energy diagram of the Stark sublevels and correlate the energy gap between the ground and the first excited states taken from the luminescence with the effective energy barriers obtained from the dynamic magnetic measurements.

Author Contributions

Conceptualization, J.L., A.A.T.; synthesis, A.A.S., D.M.L., A.A.Tyu; methodology, A.A.T., J.L and Y.G.; validation, A.A.T., J.L., G.F., I.V.T; formal analysis, S.S, G.F. A.V.C. investigation, S.S, G.F., A.V.C., I.V.T. , M.T.M., Yu.V.N.; resources, A.A.T., J.L., I.V.T. and Y.G.; data curation, G.F., A.V.C.; writing—original draft preparation, A.A.T, J.L., G.F., A.V.C, I.V.T.; writing—review and editing, G.F., J.L. and Y.G., A.V.C.; visualization, J.L., A.A.T., M.T.M. and Y.G.; supervision, A.A.T., S.S. G.F., J.L., I.V.T. and Y.G.; project administration, J.L., A.A.T and Y.G.; funding acquisition, J.L., A.A.T. and Y.G. All authors have read and agreed to the published version of the manuscript.

Conflicts of interest

There are no conflicts to declare.

Acknowledgements

The financial support of the Russian Science Foundation is highly acknowledged (Project № 17-73-30036-П). Single crystal X-ray diffraction data were collected using the equipment of the Center for molecular composition studies of INEOS RAS with financial support from the Ministry of Science and Higher Education of the Russian Federation (Contract/agreement No. 075-00697-22-00). J.L., S.S., G.F., Y.G. thank the University of Montpellier and CNRS, as well as INC CNRS International Research Program. Authors are grateful to Platform of Analysis and Characterization (PAC) of ICGM for magnetic measurements.

Notes and references

1 F.-S. Guo, B. M. Day, Y.-C. Chen, M.-L. Tong, A. Mansikkamäki and R. A. Layfield, *Science*, 2018, **362**, 1400–1403.
2 K. R. McClain, C. A. Gould, K. Chakarawet, S. J. Teat, T. J. Groshens, J. R. Long and B. G. Harvey, *Chemical Science*, 2018, **9**, 8492–8503.
3 C. A. P. Goodwin, F. Ortu, D. Reta, N. F. Chilton and D. P. Mills, *Nature*, 2017, **548**, 439–442.
4 F.-S. Guo, B. M. Day, Y.-C. Chen, M.-L. Tong, A. Mansikkamäki and R. A. Layfield, *Angew Chem Int Ed Engl*, 2017, **56**, 11445–11449.
5 S. Sanvito and A. R. Rocha, 2006.
6 A. Gaita-Ariño, F. Luis, S. Hill and E. Coronado, *Nat Chem*, 2019, **11**, 301–309.
7 L. Bogani and W. Wernsdorfer, *Nature Mater*, 2008, **7**, 179–186.
8 Y.-S. Ding, T. Han, Y.-Q. Zhai, D. Reta, N. F. Chilton, R. E. P. Winpenny and Y.-Z. Zheng, *Chemistry – A European Journal*, 2020, **26**, 5893–5902.
9 S. K. Gupta, T. Rajeshkumar, G. Rajaraman and R. Murugavel, *Chem. Sci.*, 2016, **7**, 5181–5191.
10 J. Liu, Y.-C. Chen, J.-L. Liu, V. Vieru, L. Ungur, J.-H. Jia, L. F. Chibotaru, Y. Lan, W. Wernsdorfer, S. Gao, X.-M. Chen and M.-L. Tong, *J. Am. Chem. Soc.*, 2016, **138**, 5441–5450.
11 C. Wang, R. Sun, Y. Chen, B.-W. Wang, Z.-M. Wang and S. Gao, *CCS Chemistry*, 2020, **2**, 362–368.
12 N. F. Chilton, C. A. P. Goodwin, D. P. Mills and R. E. P. Winpenny, *Chem. Commun.*, 2014, **51**, 101–103.
13 D. N. Woodruff, R. E. P. Winpenny and R. A. Layfield, *Chem. Rev.*, 2013, **113**, 5110–5148.
14 S.-D. Jiang, B.-W. Wang, H.-L. Sun, Z.-M. Wang and S. Gao, *J. Am. Chem. Soc.*, 2011, **133**, 4730–4733.
15 K. R. Meihaus and J. R. Long, *J. Am. Chem. Soc.*, 2013, **135**, 17952–17957.

16 L. Ungur, J. J. Le Roy, I. Korobkov, M. Murugesu and L. F. Chibotaru, *Angewandte Chemie International Edition*, 2014, **53**, 4413–4417.
17 J. J. L. Roy, I. Korobkov and M. Murugesu, *Chem. Commun.*, 2014, **50**, 1602–1604.
18 S.-D. Jiang, S.-S. Liu, L.-N. Zhou, B.-W. Wang, Z.-M. Wang and S. Gao, *Inorg. Chem.*, 2012, **51**, 3079–3087.
19 J. J. Le Roy, L. Ungur, I. Korobkov, L. F. Chibotaru and M. Murugesu, *J. Am. Chem. Soc.*, 2014, **136**, 8003–8010.
20 J. D. Hilgar, M. G. Bernbeck and J. D. Rinehart, *Journal of the American Chemical Society*, , DOI:10.1021/jacs.8b13514.
21 S.-M. Chen, J. Xiong, Y.-Q. Zhang, Q. Yuan, B.-W. Wang and S. Gao, *Chem. Sci.*, 2018, **9**, 7540–7545.
22 P. Zhang, L. Zhang, C. Wang, S. Xue, S.-Y. Lin and J. Tang, *J. Am. Chem. Soc.*, 2014, **136**, 4484–4487.
23 P. Zhang, J. Jung, L. Zhang, J. Tang and B. Le Guennic, *Inorg. Chem.*, 2016, **55**, 1905–1911.
24 H. Zhang, R. Nakanishi, K. Katoh, B. K. Breedlove, Y. Kitagawa and M. Yamashita, *Dalton Trans.*, 2018, **47**, 302–305.
25 K. Rogacz, M. Brzozowska, S. Baś, K. Kurpiewska and D. Pinkowicz, *Inorg. Chem.*, 2022, **61**, 16295–16306.
26 J. Long, D. M. Lyubov, A. A. Kissel', I. A. Gogolev, A. A. Tyutyunov, Y. V. Nelyubina, F. Salles, Y. Guari, A. V. Cherkasov, J. Larionova and A. A. Trifonov, *CrystEngComm*, 2022, **24**, 6953–6963.
27 A. J. Brown, D. Pinkowicz, M. R. Saber and K. R. Dunbar, *Angewandte Chemie International Edition*, 2015, **54**, 5864–5868.
28 M. Brzozowska, G. Handzlik, K. Kurpiewska, M. Zychowicz and D. Pinkowicz, *Inorg. Chem. Front.*, 2021, **8**, 2817–2828.
29 Q.-Q. Yang, Y.-F. Wang, Y.-X. Wang, M.-J. Tang and B. Yin, *Phys. Chem. Chem. Phys.*, 2023, **25**, 18387–18399.
30 Q.-C. Luo, N. Ge, Y.-Q. Zhai, T. Wang, L. Sun, Q. Sun, F. Li, Z. Fu and Y.-Z. Zheng, *Chinese Chemical Letters*, , DOI:10.1016/j.cclet.2022.05.061.
31 C. Das, A. Upadhyay, S. Vaidya, S. K. Singh, G. Rajaraman and M. Shanmugam, *Chem. Commun.*, 2015, **51**, 6137–6140.
32 S. P. Petrosyants, K. A. Babeshkin, A. V. Gavrikov, A. B. Ilyukhin, E. V. Belova and N. N. Efimov, *Dalton Trans.*, 2019, **48**, 12644–12655.
33 A. Yamashita, A. Watanabe, S. Akine, T. Nabeshima, M. Nakano, T. Yamamura and T. Kajiwara, *Angewandte Chemie International Edition*, 2011, **50**, 4016–4019.
34 J. Long, Y. Guari, R. A. S. Ferreira, L. D. Carlos and J. Larionova, *Coordination Chemistry Reviews*, 2018, **363**, 57–70.
35 J.-H. Jia, Q.-W. Li, Y.-C. Chen, J.-L. Liu and M.-L. Tong, *Coordination Chemistry Reviews*, 2019, **378**, 365–381.
36 F. Pointillart, O. Cador, B. Le Guennic and L. Ouahab, *Coordination Chemistry Reviews*, 2017, **346**, 150–175.
37 R. Marin, G. Brunet and M. Murugesu, *Angewandte Chemie International Edition*, 2021, **60**, 1728–1746.
38 L. Ungur and L. F. Chibotaru, *Chemistry – A European Journal*, 2017, **23**, 3708–3718.
39 A. F. Rogozhin, L. I. Silantyeva, A. N. Yablonskiy, B. A. Andreev, I. D. Grishin and V. A. Ilichev, *Optical Materials*, 2021, **118**, 111241.
40 P. Martín-Ramos, M. Ramos Silva, J. T. Coutinho, L. C. J. Pereira, P. Chamorro-Posada and J. Martín-Gil, *European Journal of Inorganic Chemistry*, 2014, **2014**, 511–517.
41 M. R. Silva, P. Martín-Ramos, J. T. Coutinho, L. C. J. Pereira and J. Martín-Gil, *Dalton Trans.*, 2014, **43**, 6752–6761.
42 P. Martín-Ramos, J. T. Coutinho, M. R. Silva, L. C. J. Pereira, F. Lahoz, P. S. P. da Silva, V. Lavín and J. Martín-Gil, *New J. Chem.*, 2015, **39**, 1703–1713.
43 M. Nie, J. Xiong, C. Zhao, H. Meng, K. Zhang, Y. Han, J. Li, B. Wang, L. Feng, C. Wang and T. Wang, *Nano Res.*, 2019, **12**, 1727–1731.
44 Q. Zou, X.-D. Huang, J.-C. Liu, S.-S. Bao and L.-M. Zheng, *Dalton Trans.*, 2019, **48**, 2735–2740.
45 J.-R. Jiménez, I. F. Díaz-Ortega, E. Ruiz, D. Aravena, S. J. A. Pope, E. Colacio and J. M. Herrera, *Chemistry – A European Journal*, 2016, **22**, 14548–14559.
46 K. Fan, S.-S. Bao, R. Huo, X.-D. Huang, Y.-J. Liu, Z.-W. Yu, M. Kurmoo and L.-M. Zheng, *Inorg. Chem. Front.*, 2020, **7**, 4580–4592.
47 L. Chen, J. Zhou, A. Yuan and Y. Song, *Dalton Trans.*, 2017, **46**, 15812–15818.

48 M. R. Silva, P. Martín-Ramos, J. T. Coutinho, L. C. J. Pereira, V. Lavín, I. R. Martín, P. S. P. Silva and J. Martín-Gil, *Dalton Trans.*, 2014, **44**, 1264–1272.
49 N. Monni, J. J. Baldoví, V. García-López, M. Oggianu, E. Cadoni, F. Quochi, M. Clemente-León, M. L. Mercuri and E. Coronado, *Chem. Sci.*, 2022, **13**, 7419–7428.
50 B. Liu, H. Jin, Z.-A. Kuang, X. Chen, Y.-S. Meng, S. Lin and S.-S. Liu, *Inorganica Chimica Acta*, 2020, **501**, 119297.
51 S. G. Dogaheh, H. Khanmohammadi and E. C. Sañudo, *New J. Chem.*, 2017, **41**, 10101–10111.
52 M. Ren, S.-S. Bao, R. A. S. Ferreira, L.-M. Zheng and L. D. Carlos, *Chem. Commun.*, 2014, **50**, 7621–7624.
53 J.-C. G. Bünzli, *Coordination Chemistry Reviews*, 2015, **293–294**, 19–47.
54 A. N. Carneiro Neto, E. E. S. Teotonio, G. F. de Sá, H. F. Brito, J. Legendziewicz, L. D. Carlos, M. C. F. C. Felinto, P. Gawryszewska, R. T. Moura, R. L. Longo, W. M. Faustino and O. L. Malta, in *Handbook on the Physics and Chemistry of Rare Earths*, eds. J.-C. G. Bünzli and V. K. Pecharsky, Elsevier, 2019, vol. 56, pp. 55–162.
55 F. Habib, G. Brunet, V. Vieru, I. Korobkov, L. F. Chibotaru and M. Murugesu, *J. Am. Chem. Soc.*, 2013, **135**, 13242–13245.
56 K. Reichenbächer, H. I. Süss and J. Hulliger, *Chem. Soc. Rev.*, 2005, **34**, 22–30.
57 L. Gu and R. Wu, *Phys. Rev. B*, 2021, **103**, 014401.
58 M. Briganti, F. Santanni, L. Tesi, F. Totti, R. Sessoli and A. Lunghi, *J. Am. Chem. Soc.*, 2021, **143**, 13633–13645.
59 A. Lunghi, F. Totti, S. Sanvito and R. Sessoli, *Chem. Sci.*, 2017, **8**, 6051–6059.
60 A. Lunghi and S. Sanvito, *Science Advances*, 2019, **5**, eaax7163.
61 L. Gu and R. Wu, *Phys. Rev. Lett.*, 2020, **125**, 117203.
62 Y. Ma, Y.-Q. Zhai, Q.-C. Luo, Y.-S. Ding and Y.-Z. Zheng, *Angewandte Chemie International Edition*, 2022, **61**, e202206022.
63 Q.-C. Luo and Y.-Z. Zheng, *Trends in Chemistry*, 2023, **5**, 869–872.
64 B.-K. Ling, Y.-Q. Zhai, J. Han, T. Han and Y.-Z. Zheng, *Dalton Trans.*, 2020, **49**, 6969–6973.
65 B.-K. Ling, Y.-Q. Zhai, P.-B. Jin, H.-F. Ding, X.-F. Zhang, Y. Lv, Z. Fu, J. Deng, M. Schulze, W. Wernsdorfer and Y.-Z. Zheng, *Matter*, 2022, **5**, 3485–3498.
66 D. G. Gilheany, *Chem. Rev.*, 1994, **94**, 1339–1374.
67 J. F. Kögel, A. Y. Timoshkin, A. Schröder, E. Lork and J. Beckmann, *Chem. Sci.*, 2018, **9**, 8178–8183.
68 T. J. Boyle, M. L. Neville, J. M. Sears, R. E. Cramer, M. A. Rodriguez, T. M. Alam and S. P. Bingham, *Polyhedron*, 2016, **118**, 52–60.
69 F. Huang, X. Liu, L. Hu and D. Chen, *Sci Rep*, 2014, **4**, 5053.
70 L. Sun, Y. Qiu, T. Liu, J. Z. Zhang, S. Dang, J. Feng, Z. Wang, H. Zhang and L. Shi, *ACS Appl. Mater. Interfaces*, 2013, **5**, 9585–9593.
71 S. Harder, C. Ruspic, N. N. Bhriain, F. Berkermann and M. Schürmann, *Zeitschrift für Naturforschung B*, 2008, **63**, 267–274.
72 W. A. Herrmann, R. Anwander, F. C. Munck, W. Scherer, V. Dufaud, N. W. Huber and G. R. J. Artus, *Zeitschrift für Naturforschung B*, 1994, **49**, 1789–1797.
73 S. V. Kulkarni, Ralph. Schure and Robert. Filler, *J. Am. Chem. Soc.*, 1973, **95**, 1859–1864.
74 K. Searles, B. L. Tran, M. Pink, C.-H. Chen and D. J. Mindiola, *Inorg. Chem.*, 2013, **52**, 11126–11135.
75 S. J. Lyle and Md. M. Rahman, *Talanta*, 1963, **10**, 1177–1182.
76 G. M. Sheldrick, *Acta Cryst A*, 2015, **71**, 3–8.
77 O. V. Dolomanov, L. J. Bourhis, R. J. Gildea, J. a. K. Howard and H. Puschmann, *J Appl Cryst*, 2009, **42**, 339–341.
78 G. M. Sheldrick, *Acta Cryst A*, 2008, **64**, 112–122.